

Subspace-Based Distorted-Rytov Iterative Method for Solving Inverse Scattering Problems

Tiantian Yin¹, Li Pan¹, Member, IEEE, and Xudong Chen¹, Fellow, IEEE

Abstract—In this article, an iterative method, called the subspace-based distorted-Rytov iterative method (S-DRIM), is proposed for solving inverse scattering problems. In each iteration of the S-DRIM, the subspace-Rytov approximation (SRA) is applied and the results are used to update the parameters of the background medium. Through simulations, the approximation errors of both the Rytov Approximation (RA) and the SRA in various background media are analyzed and compared. The performance of S-DRIM is verified using both synthetic and experiment data. It is observed that the S-DRIM outperforms the non-iterative SRA inversion method for the reconstructions of mild scatterers. In addition, the S-DRIM presents a smaller value of reconstruction error in optimization processes compared to the distorted-Rytov iterative method (DRIM).

Index Terms—Distorted Rytov approximation (RA), inhomogeneous background, inverse scattering.

I. INTRODUCTION

INVERSE scattering problems have garnered increasing attention in different areas such as medical examinations, nondestructive testing, oil reservoir exploration, etc.

Traditional non-iterative methods include linear inversion algorithms such as the Born approximation (BA) inversion method [1], Rytov approximation (RA) inversion method [2], [3], and back-propagation inversion method [4]. In particular, the RA has been widely applied in different scenarios such as X-ray imaging [5], [6], optical tomography [7], optical phase retrieval [8], geophysics [9], transmission lines [10], etc. These linear inversion methods are useful for solving large-scale practical problems due to low computational cost and are commonly used to provide initial profiles for iterative methods, but they also have a limited validity range. To extend the validity range, different improvements have been made based on the BA and RA inversion methods. The BA inversion method has been enhanced by several variants such as extended BA [11], modified BA inversion methods [12], and hybrid inversion methods [13].

Manuscript received 31 December 2022; revised 17 July 2023; accepted 31 July 2023. Date of publication 18 August 2023; date of current version 6 October 2023. This work was supported in part by the Singapore Ministry of Education Tier 2 Grant under Project MOE2019-T2-1-117. (Corresponding author: Xudong Chen.)

Tiantian Yin and Xudong Chen are with the Department of Electrical and Computer Engineering, National University of Singapore, Singapore 117583 (e-mail: e0021489@nus.edu; elechenx@nus.edu.sg).

Li Pan is with the Singapore Research Center, Huawei International Pte. Ltd., Singapore 138589 (e-mail: mr.panli@gmail.com).

Color versions of one or more figures in this article are available at <https://doi.org/10.1109/TAP.2023.3305327>.

Digital Object Identifier 10.1109/TAP.2023.3305327

In comparison, the RA is usually improved by retaining the neglected integral term. Considering only the first-order ray in the homogeneous low lossy scatterer for high-frequency incidences, an extended RA inversion method is proposed in [14], which greatly increases the validity range compared to the first-order RA. Using a truncated integral domain (TID) and an approximated induced current based on subspace method, the subspace-RA (SRA) inversion method is proposed in [15].

For strong scatterers, the assumptions made in the non-iterative inversion methods no longer hold, and thus the iterative methods [16], [17], [18], [19], [20], [21], [22], [23], [24], [25], [26], [27], [28], [29], [30], [31], [32], [33] or machine learning techniques [34] become indispensable. Among the commonly used iterative algorithms, one kind of algorithms is based on the linearly approximated scattering model in an iteratively updated background [35] including distorted Born iterative method (DBIM) [20], distorted Rytov iterative method (DRIM) for both full data [21], [22], and phaseless data [23], [24]. The convergence rate of DBIM is further improved in subspace-DBIM (S-DBIM) [36]. Under RA, a branch-and-bound algorithm is proposed in [31]. By using an improved RA for the representation of total electric field in the data equation, an iterative method is proposed in [25]. Based on the extended RA non-iterative inversion method [14], an iterative algorithm for phaseless data is proposed in [26].

In this article, an iterative method, called the subspace-based DRIM (S-DRIM), is proposed for solving inverse scattering problems. In each iteration of the S-DRIM, the SRA is used for the inversions and the background medium is updated iteratively. The contributions of this article are as follows. First, the approximation errors of the RA and the SRA in the background are analyzed and compared. It is observed that the SRA is more accurate than the RA when the difference between the permittivity distributions of the scatterer and the background medium is large. However, the difference between the approximation errors of the RA and the SRA decreases as the difference between the permittivity distributions of the scatterer and the background medium decreases, which indicates that when the difference between the permittivity distributions of the scatterer and the background medium is small, the RA is also an accurate approximation. Second, the S-DRIM is compared with the non-iterative SRA inversion method. It is observed that the S-DRIM could better reconstruct mild scatterers compared to the non-iterative SRA inversion method because the non-iterative SRA inversion

method is the first step of the S-DRIM. Third, the performance of the DRIM and the S-DRIM is compared using both synthetic and experiment data. It is found that the S-DRIM converges to a similar value as the DRIM but at a faster speed. It is consistent with the observation that the advantage of the SRA gradually vanishes when the difference between the permittivity distributions of the true scatterer and the background medium is getting smaller. Fourth, this article provides new definitions of the approximation errors of the RA and the SRA, which avoids the phase wrapping problems for strong scatterers.

The article is structured as follows. In Section II, the forward problem is introduced. In addition, the formulations of the RA and the SRA in a general background medium, the corresponding newly defined approximation errors, the DRIM, and the S-DRIM are also given in Section II. The comparisons between the newly defined errors and the inversion results of different methods are provided in Section III. The conclusions are drawn in Section IV.

II. FORMULATIONS

A. Forward Problem

Consider a 2-D transverse magnetic (TM) scenario. The forward problem is to find the scattered field observed in domain S , given the permittivity distribution in the domain of interest (DOI) D . We divide the whole space into S and D in such a way that S consists of only free space and all scatterers are in D . In the first step of the forward problem, the total electric field within the DOI is calculated using

$$E_t(\mathbf{r}) = E_{\text{inc}}(\mathbf{r}) + i\omega\mu_0 \int \int_D g(\mathbf{r}, \mathbf{r}') \chi_o(\mathbf{r}') E_t(\mathbf{r}') d\mathbf{r}' \quad (1)$$

where ω is the angular frequency, μ_0 is the permeability of the free space, $g(\mathbf{r}, \mathbf{r}')$ is the Green's function in the free space, $E_t(\mathbf{r})$ is the total electric field, $E_{\text{inc}}(\mathbf{r})$ is the incident field and the normalized contrast of the scatterer is $\chi_o(\mathbf{r}') = -i\omega\epsilon_0(\epsilon_{\text{or}}(\mathbf{r}') - 1)$, ϵ_0 is the permittivity of the free space, and $\epsilon_{\text{or}}(\mathbf{r}')$ is the relative permittivity distribution of the scatterer, $\mathbf{r}, \mathbf{r}' \in D$. In the second step, using the total electric field $E_t(\mathbf{r}')$ obtained in the first step, the scattered field E_s at \mathbf{r}_s in S is obtained using

$$E_s(\mathbf{r}_s) = i\omega\mu_0 \int \int_D g(\mathbf{r}_s, \mathbf{r}) \chi_o(\mathbf{r}) E_t(\mathbf{r}) d\mathbf{r}. \quad (2)$$

By discretizing the DOI into M_{DOI} pixels, (1) and (2), which correspond to the two steps of the forward problem, can be numerically written as

$$\bar{E}_t = \bar{E}_{\text{inc}} + \bar{\bar{G}}_D \cdot \bar{\bar{\chi}}_o \cdot \bar{E}_t \quad (3)$$

and

$$\bar{E}_s = \bar{\bar{G}}_s \cdot \bar{\bar{\chi}}_o \cdot \bar{E}_t \quad (4)$$

respectively, where $\bar{\bar{\chi}}_o$ is a diagonal matrix.

B. RA in a General Background

The inverse scattering problem is to find the distribution of normalized contrast χ_o in DOI, given the scattered field observed in S and the incident field in DOI, it can be solved by minimizing a cost function, in the form of

$$f(\chi_{\text{rec}}) = \sum_{p=1}^{N_i} \|S^p(\chi_{\text{rec}}) - E_s^p\|^2 + \beta T(\chi_{\text{rec}}) \quad (5)$$

where S^p is an operator mapping the normalized contrast of the scatterer to the scattered field in S for the p th incidence, for $p = 1, 2, \dots, N_i$, N_i is the total number of incidences, β is the regularization coefficient, and $T(\cdot)$ is the regularization function. DRIM is one of the commonly used iterative methods for solving inverse scattering problems, where RA inversion is performed in each iteration and its result is used to update the background medium.

Throughout this article, we often refer to the concept of general background, which could be inhomogeneous. The normalized contrast of the background is defined as $\chi_b(\mathbf{r}) = -i\omega\epsilon_0[\epsilon_{\text{br}}(\mathbf{r}) - 1]$ and the normalized contrast of the scatterer is defined as $\chi_o(\mathbf{r}) = -i\omega\epsilon_0[\epsilon_{\text{or}}(\mathbf{r}) - \epsilon_{\text{br}}(\mathbf{r})]$. In each iteration, the former is known and the latter is to be found. Note that the general background is usually different from the background identified based on common sense. In a general background medium, the scattering phenomenon as in [11] is described by

$$E_b(\mathbf{r})\psi(\mathbf{r}) = \int \int_D g_b(\mathbf{r}, \mathbf{r}') i\omega\mu_0 \chi_o(\mathbf{r}') E_b(\mathbf{r}') d\mathbf{r}' + \int_{-\infty}^{\infty} \int_{-\infty}^{\infty} g_b(\mathbf{r}, \mathbf{r}') [\nabla' \psi(\mathbf{r}')]^2 E_b(\mathbf{r}') d\mathbf{r}' \quad (6)$$

where $E_b(\mathbf{r})$ is the total field in the background in the absence of the scatterer, $\psi(\mathbf{r})$ is defined to satisfy

$$E_t(\mathbf{r}) = E_b(\mathbf{r})e^{\psi(\mathbf{r})}. \quad (7)$$

The background Green's function $g_b(\mathbf{r}, \mathbf{r}')$ is the solution of

$$\nabla^2 g_b(\mathbf{r}, \mathbf{r}') + k_b(\mathbf{r})^2 g_b(\mathbf{r}, \mathbf{r}') = -\delta(\mathbf{r} - \mathbf{r}') \quad (8)$$

where $k_b(\mathbf{r})$ is the wavenumber of the general background medium and $k_b(\mathbf{r})^2 = \omega^2 \epsilon_0 \mu_0 \epsilon_{\text{br}}(\mathbf{r})$. The analytical expression of $g_b(\mathbf{r}, \mathbf{r}')$ is given as

$$g_b(\mathbf{r}, \mathbf{r}') = g(\mathbf{r}, \mathbf{r}') (I - \chi_b G_D)^{-1} \quad (9)$$

where G_D is the operator mapping from the induced current to the scattered field within the DOI in the free space background.

When $[\nabla' \psi(\mathbf{r}')]^2 \ll i\omega\mu_0 \chi_o(\mathbf{r}')$ is satisfied for weak scatterers, the second integral in (6) can be neglected and the RA is valid, which is

$$E_b(\mathbf{r})\psi(\mathbf{r}) \approx \int \int_D g_b(\mathbf{r}, \mathbf{r}') i\omega\mu_0 \chi_o(\mathbf{r}') E_b(\mathbf{r}') d\mathbf{r}'. \quad (10)$$

C. SRA in a General Background

In the free space background, it has been demonstrated that the SRA [15], in which the infinite integral domain of the second integral in (6) is truncated using a TID as shown in Fig. 1 and $[\nabla' \psi(\mathbf{r}')]^2$ in the integrand is approximated

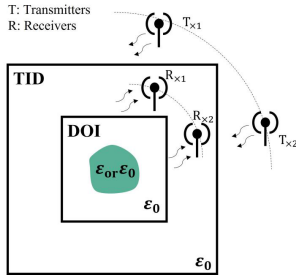


Fig. 1. Illustration of DOI and TID.

by $[\nabla'\psi^+(\mathbf{r}')]^2$, is more accurate than the RA for relatively strong scatterers. To compare the performance of the RA and the SRA in a general background, which could be inhomogeneous, the formulation of the SRA in a general background is provided in this section.

In a general background with relative permittivity distribution of $\varepsilon_{\text{br}}(\mathbf{r})$, by truncating the integral domain of the second integral in (6) using a TID and approximating $[\nabla'\psi(\mathbf{r}')]^2$ in the integrand by $[\nabla'\psi^+(\mathbf{r}')]^2$, the formulation of the SRA is given as

$$\begin{aligned} E_b(\mathbf{r})\psi(\mathbf{r}) \approx & \int \int_D g_b(\mathbf{r}, \mathbf{r}') i\omega\mu_0\chi_o(\mathbf{r}') E_b(\mathbf{r}') d\mathbf{r}' \\ & + \int \int_{\text{TID}} g_b(\mathbf{r}, \mathbf{r}') [\nabla'\psi^+(\mathbf{r}')]^2 E_b(\mathbf{r}') d\mathbf{r}'. \end{aligned} \quad (11)$$

The evaluation of $[\nabla'\psi^+(\mathbf{r}')]^2$ in a general background will be given in Section II-F.

D. Approximation Error of RA in a General Background

In the section, the approximation error of the RA in a general background is quantified.

After discretization, (10) becomes

$$\bar{E}_{b,R} \cdot \bar{\psi}_R \approx \bar{\bar{G}}_{bs} \cdot \bar{\bar{E}}_b \cdot \bar{\chi}_o \quad (12)$$

where subscript R means that the quantities are evaluated at the N_s receivers. $\bar{E}_{b,R}$ is a diagonal matrix of size $N_s \times N_s$, $\bar{\psi}_R$ is a vector of length N_s and it is defined as

$$\bar{E}_{t,R}(n) = \bar{\bar{E}}_{b,R}(n, n) e^{\bar{\psi}_R(n)} \quad (13)$$

where $n = 1, 2, \dots, N_s$. $\bar{\bar{E}}_b$ is a diagonal matrix of size $M_{\text{DOI}} \times M_{\text{DOI}}$, $\bar{\chi}_o$ is a vector of length M_{DOI} . $\bar{\bar{G}}_{bs}$, which is of size $N_s \times M_{\text{DOI}}$, is defined according to (9) as

$$\bar{\bar{G}}_{bs} = \bar{\bar{G}}_s \cdot (\bar{\bar{I}} - \bar{\bar{\chi}}_b \cdot \bar{\bar{G}}_D)^{-1} \quad (14)$$

where $\bar{\bar{\chi}}_b$ is an $M_{\text{DOI}} \times M_{\text{DOI}}$ diagonal matrix of the normalized contrast of the background, which is defined as $\bar{\bar{\chi}}_b = -i\omega\varepsilon_0(\bar{\varepsilon}_{\text{br}} - \bar{\bar{I}})$. In order to avoid the phase-wrapping problems brought about by calculating the natural logarithm function in $\bar{\psi}_R$, (12) is rewritten as

$$\bar{E}_{t,R}(n) \approx \bar{\bar{E}}_{b,R}(n, n) \cdot \exp \left[\bar{\bar{E}}_{b,R}(n, n)^{-1} \cdot \left(\bar{\bar{G}}_{bs}^n \right)^T \cdot \bar{\bar{E}}_b \cdot \bar{\chi}_o \right] \quad (15)$$

where $(\bar{\bar{G}}_{bs}^n)^T$ is the n th row of the matrix $\bar{\bar{G}}_{bs}$. According to (15), the error of the RA in the background is defined as

$$err_0 = \frac{\|\bar{\bar{Q}}_{\text{nom}0}\|}{\|\bar{\bar{Q}}_{\text{den}}\|} \quad (16)$$

where

$$\begin{aligned} \bar{\bar{Q}}_{\text{nom}0}(n) = & \bar{E}_{t,R}(n) - \bar{\bar{E}}_{b,R}(n, n) \\ & \cdot \exp \left[\bar{\bar{E}}_{b,R}(n, n)^{-1} \cdot \left(\bar{\bar{G}}_{bs}^n \right)^T \cdot \bar{\bar{E}}_b \cdot \bar{\chi}_o \right] \end{aligned} \quad (17)$$

and

$$\bar{\bar{Q}}_{\text{den}}(n) = \bar{E}_{t,R}(n). \quad (18)$$

E. First Approximation Error of SRA in a General Background

In the DRIM, the RA inversion method, in which the second integral in (6) is neglected, is performed in each iteration. In order to retain the second integral in (6) in the iterative inversion algorithm, the approximation errors of using a TID for the retained term in the background are of great interest. Using an accurate $[\nabla'\psi(\mathbf{r}')]^2$ and a TID for the second integral in (6), after discretizing the TID into M_{TID} pixels, it is obtained that

$$\bar{\bar{E}}_{b,R} \cdot \bar{\psi}_R - \frac{1}{i\omega\mu_0} \bar{\bar{G}}_{bs,\text{TID}} \cdot \bar{\bar{P}}_{1,\text{TID}} \cdot \bar{E}_{b,\text{TID}} \approx \bar{\bar{G}}_{bs} \cdot \bar{\bar{E}}_b \cdot \bar{\chi}_o \quad (19)$$

where the matrices or the vectors with the subscript of TID are evaluated in the TID, $\bar{\bar{P}}_{1,\text{TID}}$ is given in Table I. $\bar{E}_{b,\text{TID}}$ is a vector of length M_{TID} . $\bar{\bar{G}}_{bs,\text{TID}}$, which is of size $N_s \times M_{\text{TID}}$, is defined as

$$\bar{\bar{G}}_{bs,\text{TID}} = \bar{\bar{G}}_{s,\text{TID}} \cdot (\bar{\bar{I}} - \bar{\bar{\chi}}_{b,\text{TID}} \cdot \bar{\bar{G}}_{D,\text{TID}})^{-1} \quad (20)$$

where

$$\begin{aligned} \bar{\bar{G}}_{s,\text{TID}}(n, m) = & \begin{cases} \frac{-\eta\pi a}{2} J_1(k_0 a) H_0^{(1)} \left(k_0 \bar{\bar{R}}_{R-\text{TID}}(n, m) \right), & \text{if } \bar{\bar{R}}_{R-\text{TID}}(n, m) > a \\ \frac{-\eta\pi a}{2} H_1^{(1)}(k_0 a) - \frac{i\eta}{k_0}, & \text{if } \bar{\bar{R}}_{R-\text{TID}}(n, m) \leq a \end{cases} \end{aligned} \quad (21)$$

where $n = 1, 2, \dots, N_s$, $m = 1, 2, \dots, M_{\text{TID}}$. $\bar{\bar{R}}_{R-\text{TID}}(nm)$ is the distance between the n th receiver and the center of the m th pixel in the TID. $\bar{\bar{G}}_{D,\text{TID}}$ is defined in the same way as $\bar{\bar{G}}_{D,\text{X}_b,\text{TID}}$ is an $M_{\text{TID}} \times M_{\text{TID}}$ diagonal matrix. To avoid the phase-wrapping problems, (19) is rewritten as

$$\begin{aligned} \bar{E}_{t,R}(n) & \approx \bar{\bar{E}}_{b,R}(n, n) \\ & \approx \bar{\bar{E}}_{b,R}(n, n) \cdot \exp \left[\bar{\bar{E}}_{b,R}(n, n)^{-1} \cdot \frac{1}{i\omega\mu_0} \left(\bar{\bar{G}}_{bs,\text{TID}}^n \right)^T \cdot \bar{\bar{P}}_{1,\text{TID}} \cdot \bar{E}_{b,\text{TID}} \right. \\ & \quad \left. + \bar{\bar{E}}_{b,R}(n, n)^{-1} \cdot \left(\bar{\bar{G}}_{bs}^n \right)^T \cdot \bar{\bar{E}}_b \cdot \bar{\chi}_o \right] \end{aligned} \quad (22)$$

TABLE I

DEFINITIONS OF DIFFERENT MATRICES. ($m, m' = 1, 2, \dots, M_{\text{TID}}$)

$\bar{\bar{P}}_{1,\text{TID}}(m, m)$	$= \left[\begin{array}{l} \left[\bar{G}_{x,\text{TID}}^m \cdot (\bar{I} - \bar{\bar{\chi}}_{b,\text{TID}} \cdot \bar{\bar{G}}_{D,\text{TID}})^{-1} \cdot \bar{J}_{\text{TID}} \cdot \bar{E}_{b,\text{TID}}(m) \right]^2 \\ -ik \cos(\theta_{\text{inc}}) \bar{E}_{\text{inc},\text{TID}}(m) \bar{E}_{s,\text{TID}}(m) \\ -\bar{G}_{x,\text{TID}}^m \cdot \bar{\bar{\chi}}_{b,\text{TID}} \cdot \bar{E}_{b,\text{TID}} \cdot \bar{E}_{s,\text{TID}}(m) \end{array} \right] \\ + \left[\begin{array}{l} \left[\bar{G}_{y,\text{TID}}^m \cdot (\bar{I} - \bar{\bar{\chi}}_{b,\text{TID}} \cdot \bar{\bar{G}}_{D,\text{TID}})^{-1} \cdot \bar{J}_{\text{TID}} \cdot \bar{E}_{b,\text{TID}}(m) \right]^2 \\ -ik \sin(\theta_{\text{inc}}) \bar{E}_{\text{inc},\text{TID}}(m) \bar{E}_{s,\text{TID}}(m) \\ -\bar{G}_{y,\text{TID}}^m \cdot \bar{\bar{\chi}}_{b,\text{TID}} \cdot \bar{E}_{b,\text{TID}} \cdot \bar{E}_{s,\text{TID}}(m) \end{array} \right] \\ / [\bar{E}_{t,\text{TID}}(m) \cdot \bar{E}_{b,\text{TID}}(m)]^2 \end{array} \right]$
$\bar{E}_{t,\text{TID}} = \bar{E}_{b,\text{TID}} + \bar{\bar{G}}_{D,\text{TID}} \cdot \left[\bar{I} - \bar{\bar{\chi}}_{b,\text{TID}} \cdot \bar{\bar{G}}_{D,\text{TID}} \right]^{-1} \cdot \bar{J}_{\text{TID}}$	
$\bar{E}_{s,\text{TID}} = \bar{\bar{G}}_{D,\text{TID}} \cdot \left[\bar{I} - \bar{\bar{\chi}}_{b,\text{TID}} \cdot \bar{\bar{G}}_{D,\text{TID}} \right]^{-1} \cdot \bar{J}_{\text{TID}}$	
$\bar{J}_{\text{TID}} = \bar{\bar{\chi}}_{o,\text{TID}} \cdot \bar{E}_{t,\text{TID}}$	
$\bar{\bar{P}}_{2,\text{TID}}(m, m)$	$= \left[\begin{array}{l} \left[\bar{G}_{x,\text{TID}}^m \cdot (\bar{I} - \bar{\bar{\chi}}_{b,\text{TID}} \cdot \bar{\bar{G}}_{D,\text{TID}})^{-1} \cdot \bar{J}_{\text{TID}}^+ \cdot \bar{E}_{b,\text{TID}}(m) \right]^2 \\ -ik \cos(\theta_{\text{inc}}) \bar{E}_{\text{inc},\text{TID}}(m) \bar{E}_{sa,\text{TID}}(m) \\ -\bar{G}_{x,\text{TID}}^m \cdot \bar{\bar{\chi}}_{b,\text{TID}} \cdot \bar{E}_{b,\text{TID}} \cdot \bar{E}_{sa,\text{TID}}(m) \end{array} \right] \\ + \left[\begin{array}{l} \left[\bar{G}_{y,\text{TID}}^m \cdot (\bar{I} - \bar{\bar{\chi}}_{b,\text{TID}} \cdot \bar{\bar{G}}_{D,\text{TID}})^{-1} \cdot \bar{J}_{\text{TID}}^+ \cdot \bar{E}_{b,\text{TID}}(m) \right]^2 \\ -ik \sin(\theta_{\text{inc}}) \bar{E}_{\text{inc},\text{TID}}(m) \bar{E}_{sa,\text{TID}}(m) \\ -\bar{G}_{y,\text{TID}}^m \cdot \bar{\bar{\chi}}_{b,\text{TID}} \cdot \bar{E}_{b,\text{TID}} \cdot \bar{E}_{sa,\text{TID}}(m) \end{array} \right] \\ / [\bar{E}_{ta,\text{TID}}(m) \cdot \bar{E}_{b,\text{TID}}(m)]^2 \end{array} \right]$
$\bar{E}_{ta,\text{TID}} = \bar{E}_{b,\text{TID}} + \bar{\bar{G}}_{D,\text{TID}} \cdot \left[\bar{I} - \bar{\bar{\chi}}_{b,\text{TID}} \cdot \bar{\bar{G}}_{D,\text{TID}} \right]^{-1} \cdot \bar{J}_{\text{TID}}^+$	
$\bar{E}_{sa,\text{TID}} = \bar{\bar{G}}_{D,\text{TID}} \cdot \left[\bar{I} - \bar{\bar{\chi}}_{b,\text{TID}} \cdot \bar{\bar{G}}_{D,\text{TID}} \right]^{-1} \cdot \bar{J}_{\text{TID}}^+$	
J_{TID}^+ is obtained by padding zeros to J^+	
$\bar{G}_{x,\text{TID}}^m(m') =$ $\left\{ \begin{array}{ll} \frac{k_0 \eta \pi a}{2} J_1(k_0 a) H_1^{(1)} \left[k_0 \bar{\bar{R}}_{\text{TID}}(m, m') \right] \frac{\bar{x}_{\text{TID}}(m) - \bar{x}_{\text{TID}}(m')}{\bar{\bar{R}}_{\text{TID}}(m, m')} , & \text{if } m \neq m' \\ 0, & \text{if } m = m' \end{array} \right.$	$\bar{\bar{E}}_{b,R} \cdot \bar{\psi}_R - \frac{1}{i \omega \mu_0} \bar{\bar{G}}_{bs,\text{TID}} \cdot \bar{\bar{P}}_{2,\text{TID}} \cdot \bar{E}_{b,\text{TID}} \approx \bar{\bar{G}}_{bs} \cdot \bar{\bar{E}}_b \cdot \bar{\chi}_o$
$\bar{G}_{y,\text{TID}}^m(m') =$ $\left\{ \begin{array}{ll} \frac{k_0 \eta \pi a}{2} J_1(k_0 a) H_1^{(1)} \left[k_0 \bar{\bar{R}}_{\text{TID}}(m, m') \right] \frac{\bar{y}_{\text{TID}}(m) - \bar{y}_{\text{TID}}(m')}{\bar{\bar{R}}_{\text{TID}}(m, m')} , & \text{if } m \neq m' \\ 0, & \text{if } m = m' \end{array} \right.$	$\bar{\bar{E}}_{t,R}(n) \approx \bar{\bar{E}}_{b,R}(n, n)$ $\cdot \exp \left[\begin{array}{l} \bar{\bar{E}}_{b,R}(n, n)^{-1} \cdot \frac{1}{i \omega \mu_0} \left(\bar{\bar{G}}_{bs,\text{TID}}^n \right)^T \cdot \bar{\bar{P}}_{2,\text{TID}} \cdot \bar{E}_{b,\text{TID}} \\ + \bar{\bar{E}}_{b,R}(n, n)^{-1} \cdot \left(\bar{\bar{G}}_{bs}^n \right)^T \cdot \bar{\bar{E}}_b \cdot \bar{\chi}_o \end{array} \right]$
$\bar{\bar{R}}_{\text{TID}}(m, m') = \sqrt{[\bar{x}_{\text{TID}}(m) - \bar{x}_{\text{TID}}(m')]^2 + [\bar{y}_{\text{TID}}(m) - \bar{y}_{\text{TID}}(m')]^2}$	

where $(\bar{\bar{G}}_{bs,\text{TID}}^n)^T$ is the n th row of the matrix $\bar{\bar{G}}_{bs,\text{TID}}$. According to (22), the approximation error of using the accurate ψ

and the TID for the second integral in (6) is defined as

$$err_1 = \frac{\|\bar{\bar{Q}}_{\text{nom1}}\|}{\|\bar{\bar{Q}}_{\text{den}}\|} \quad (23)$$

where

$$\begin{aligned} \bar{\bar{Q}}_{\text{nom1}}(n) &= \bar{E}_{t,R}(n) - \bar{\bar{E}}_{b,R}(n, n) \\ &\cdot \exp \left[\begin{array}{l} \bar{\bar{E}}_{b,R}(n, n)^{-1} \cdot \frac{1}{i \omega \mu_0} \left(\bar{\bar{G}}_{bs,\text{TID}}^n \right)^T \cdot \bar{\bar{P}}_{1,\text{TID}} \cdot \bar{E}_{b,\text{TID}} \\ + \bar{\bar{E}}_{b,R}(n, n)^{-1} \cdot \left(\bar{\bar{G}}_{bs}^n \right)^T \cdot \bar{\bar{E}}_b \cdot \bar{\chi}_o \end{array} \right] \end{aligned} \quad (24)$$

and $\bar{\bar{Q}}_{\text{den}}(n)$ is defined in (18).

F. Second Approximation Error of the SRA in a General Background

In this section, the approximation errors of using a TID and an approximated $[\nabla' \psi(\mathbf{r}')]^2$, which is denoted as $[\nabla' \psi^+(\mathbf{r}')]^2$, for the second integral in (6) in the background are quantified.

The Green's function in the background can be decomposed as $\bar{\bar{G}}_{bs} = \bar{\bar{U}} \cdot \bar{\bar{\Sigma}} \cdot \bar{\bar{V}}^H$. The induced current can be represented by the right singular vector bases, namely $\bar{j} = \bar{\bar{V}} \cdot \bar{\alpha}$, where $\bar{\alpha}$ is the vector of the current coefficients. The first L right singular vector bases represent the major induced current, and the remaining right singular vector bases represent the minor induced current. The major and the minor induced currents are given as $\bar{j}^+ = \bar{\bar{V}}^+ \cdot \bar{\alpha}^+$ and $\bar{j}^- = \bar{\bar{V}}^- \cdot \bar{\alpha}^-$, respectively. The major induced current coefficients are calculated using $\alpha_j = ((\bar{u}_j^H \cdot (\bar{E}_{t,R} - \bar{E}_{\text{inc},R} - \bar{\bar{G}}_s \cdot \bar{\bar{\chi}}_b \cdot \bar{E}_b)) / \sigma_j)$, where \bar{u}_j is the j th column of $\bar{\bar{U}}$ and σ_j is the j th diagonal element of $\bar{\bar{\Sigma}}$, and $j = 1, 2, \dots, L$. The major induced current \bar{j}^+ can be used to calculate the discretized matrix of $[\nabla' \psi^+(\mathbf{r}')]^2$ and the details are given in Table I. Using $[\nabla' \psi^+(\mathbf{r}')]^2$ and a TID for the second integral in (6), after discretization, it is obtained that

$$\bar{\bar{E}}_{b,R} \cdot \bar{\psi}_R - \frac{1}{i \omega \mu_0} \bar{\bar{G}}_{bs,\text{TID}} \cdot \bar{\bar{P}}_{2,\text{TID}} \cdot \bar{E}_{b,\text{TID}} \approx \bar{\bar{G}}_{bs} \cdot \bar{\bar{E}}_b \cdot \bar{\chi}_o \quad (25)$$

where $\bar{\bar{P}}_{2,\text{TID}}$ is defined in Table I. In order to avoid the phase-wrapping problems, (25) is rewritten as

$$\begin{aligned} \bar{E}_{t,R}(n) &\approx \bar{\bar{E}}_{b,R}(n, n) \\ &\cdot \exp \left[\begin{array}{l} \bar{\bar{E}}_{b,R}(n, n)^{-1} \cdot \frac{1}{i \omega \mu_0} \left(\bar{\bar{G}}_{bs,\text{TID}}^n \right)^T \cdot \bar{\bar{P}}_{2,\text{TID}} \cdot \bar{E}_{b,\text{TID}} \\ + \bar{\bar{E}}_{b,R}(n, n)^{-1} \cdot \left(\bar{\bar{G}}_{bs}^n \right)^T \cdot \bar{\bar{E}}_b \cdot \bar{\chi}_o \end{array} \right] \end{aligned} \quad (26)$$

where $n = 1, 2, \dots, N_s$. The approximation error of using approximated ψ and TID for the second integral in (6) is defined as

$$err_2 = \frac{\|\bar{\bar{Q}}_{\text{nom2}}\|}{\|\bar{\bar{Q}}_{\text{den}}\|} \quad (27)$$

where

$$\begin{aligned} \bar{Q}_{\text{nom2}}(n) \\ = \bar{E}_{t,R}(n) - \bar{\bar{E}}_{b,R}(n, n) \\ \cdot \exp \left[\bar{\bar{E}}_{b,R}(n, n)^{-1} \cdot \frac{1}{i\omega\mu_0} \left(\bar{G}_{\text{bs},\text{TID}}^n \right)^T \cdot \bar{\bar{P}}_{2,\text{TID}} \cdot \bar{E}_{b,\text{TID}} \right. \\ \left. + \bar{\bar{E}}_{b,R}(n, n)^{-1} \cdot \left(\bar{G}_{\text{bs}}^n \right)^T \cdot \bar{\bar{E}}_b \cdot \bar{\chi}_o \right] \end{aligned} \quad (28)$$

and $\bar{Q}_{\text{den}}(n)$ is defined in (18).

G. Distorted Rytov Iterative Method

The cost function of DRIM is defined as

$$f(\bar{\chi}_o) = \sum_{p=1}^{N_i} \left\| \bar{\bar{G}}_{\text{bs}} \cdot \bar{\bar{E}}_b^p \cdot \bar{\chi}_o - \bar{E}_{b,R}^p \cdot \bar{\psi}_R^p \right\|^2 + \left\| \bar{\bar{M}} \cdot \bar{\chi}_o \right\|^2 \quad (29)$$

where $\bar{\bar{M}}$ is a diagonal $M_{\text{DOI}} \times M_{\text{DOI}}$ matrix, which is different for different regularizations. In this article, $\bar{\bar{M}} = \beta \bar{I}$ is used. The numerical optimization algorithm is given as below:

Step 1: Initialization step, $n = 0$, set the background as free space, which is the physical background. $\bar{E}_{b,R}^{p,0} = \bar{E}_{\text{inc},R}^p$, $\bar{E}_b^{p,0} = \bar{E}_{\text{inc}}^p$. It is obtained that $\bar{\psi}_R^{p,0}(n) = \ln(\bar{E}_{t,R}^p / \bar{E}_{b,R}^{p,0}(n)) = \ln(\bar{E}_{t,R}^p / \bar{E}_{\text{inc},R}^p(n))$. The Green's function of free space is used, namely $\bar{\bar{G}}_{\text{bs}}^0 = \bar{\bar{G}}_s$. $\bar{\chi}_o^0$ is obtained by minimizing (29) and $\bar{\chi}_b^1 = \bar{\chi}_o^0$.

Step 2: $n = n + 1$

Update the secondary incident field

$$\bar{E}_b^{p,n} = (\bar{I} - \bar{\bar{G}}_D \cdot \bar{\chi}_b^n)^{-1} \cdot \bar{E}_{\text{inc}}^p \quad (30)$$

$$\bar{E}_{b,R}^{p,n} = \bar{E}_{\text{inc},R}^p + \bar{\bar{G}}_s \cdot \bar{\chi}_b^n \cdot \bar{E}_b^{p,n}. \quad (31)$$

Update $\bar{\psi}_R^{p,n}$

$$\bar{\psi}_R^{p,n}(m) = \ln \left(\bar{E}_{t,R}^p(m) / \bar{E}_{b,R}^{p,n}(m) \right). \quad (32)$$

Update $\bar{\bar{G}}_{\text{bs}}^n$

$$\bar{\bar{G}}_{\text{bs}}^n = \bar{\bar{G}}_s \cdot (\bar{I} - \bar{\chi}_b^n \cdot \bar{\bar{G}}_D)^{-1}. \quad (33)$$

Step 3: Update $\bar{\chi}_o^n$ by minimizing (29) and update the normalized contrast by

$$\bar{\chi}_b^{n+1} = \bar{\chi}_b^n + \bar{\chi}_o^n. \quad (34)$$

Step 4: If the termination condition is satisfied, end the loop. Otherwise, go to Step 2.

H. Subspace-Based DRIM

The cost function of S-DRIM is

$$\begin{aligned} f(\bar{\chi}_o) = \sum_{p=1}^{N_i} \left\| + \left(\frac{1}{i\omega\mu_0} \bar{\bar{G}}_{\text{bs},\text{TID}} \cdot \bar{\bar{P}}_{2,\text{TID}} \cdot \bar{E}_{b,\text{TID}}^p \right) \right\|^2 \\ + \left\| \bar{\bar{M}} \cdot \bar{\chi}_o \right\|^2. \end{aligned} \quad (35)$$

The numerical optimization algorithm is given as below.

Step 1: Initialization step, $n = 0$, set the background as the free space, which is the physical background. $\bar{E}_b^{p,0} = \bar{E}_{\text{inc}}^p$, $\bar{E}_{b,\text{TID}}^{p,0} = \bar{E}_{\text{inc},\text{TID}}^p$, $\bar{E}_{b,R}^{p,0} = \bar{E}_{\text{inc},R}^p$. It is obtained that $\bar{\psi}_R^{p,0}(m) = \ln(\bar{E}_{t,R}^p / \bar{E}_{b,R}^{p,0}(m)) = \ln(\bar{E}_{t,R}^p / \bar{E}_{\text{inc},R}^p(m))$. The Green's function of free space is used, namely $\bar{\bar{G}}_{\text{bs}}^0 = \bar{\bar{G}}_s$, $\bar{\bar{G}}_{\text{bs},\text{TID}}^0 = \bar{\bar{G}}_{\text{s,TID}}^0$, $\bar{\bar{G}}_{b,D,\text{TID}}^0 = \bar{\bar{G}}_{D,\text{TID}}^0$.

Conduct the thin SVD of $\bar{\bar{G}}_s$

$$\bar{\bar{G}}_s = \sum_{i=1}^{N_s} \sigma_{i,0} \cdot \bar{u}_{i,0} \cdot \bar{v}_{i,0}^H. \quad (36)$$

Calculate the major induced current

$$\bar{J}_+^{p,0} = \sum_{i=1}^L \frac{\bar{u}_{i,0}^H \cdot (\bar{E}_{t,R}^p - \bar{E}_{\text{inc},R}^p)}{\sigma_{i,0}} \bar{v}_{i,0} \quad (37)$$

where $\bar{J}_{+, \text{TID}}^{p,0}$ is obtained by padding zeros to $\bar{J}_+^{p,0}$.

Update $\bar{E}_{\text{sa},\text{TID}}^{p,0}$, $\bar{E}_{\text{ta},\text{TID}}^{p,0}$

$$\bar{E}_{\text{sa},\text{TID}}^{p,0} = \bar{\bar{G}}_{b,D,\text{TID}}^0 \cdot \bar{J}_{+, \text{TID}}^{p,0} \quad (38)$$

$$\bar{E}_{\text{ta},\text{TID}}^{p,0} = \bar{E}_{b,\text{TID}}^{p,0} + \bar{E}_{\text{sa},\text{TID}}^{p,0}. \quad (39)$$

Calculate the matrix $\bar{\bar{P}}_{2,\text{TID}}^{p,0}$

$$\begin{aligned} \bar{\bar{P}}_{2,\text{TID}}^{p,0}(m, m) \\ = \left\{ \begin{array}{l} \left[\bar{G}_{x,\text{TID}}^m T \cdot \bar{J}_{+, \text{TID}}^{p,0} \cdot \bar{E}_{\text{inc},\text{TID}}^p(m) \right]^2 \\ - ik \cos(\theta_{\text{inc}}) \cdot \bar{E}_{\text{inc},\text{TID}}^p(m) \cdot \bar{E}_{\text{sa},\text{TID}}^{p,0}(m) \\ + \left[\bar{G}_{y,\text{TID}}^m T \cdot \bar{J}_{+, \text{TID}}^{p,0} \cdot \bar{E}_{\text{inc},\text{TID}}^p(m) \right]^2 \\ - ik \sin(\theta_{\text{inc}}) \cdot \bar{E}_{\text{inc},\text{TID}}^p(m) \cdot \bar{E}_{\text{sa},\text{TID}}^{p,0}(m) \end{array} \right\} \\ / \left(\bar{E}_{\text{ta},\text{TID}}^{p,0}(m) \cdot \bar{E}_{\text{inc},\text{TID}}^p(m) \right)^2 \end{aligned} \quad (40)$$

where $\bar{G}_{x,\text{TID}}^m$, $\bar{G}_{y,\text{TID}}^m$ are given in Table I. $\bar{\chi}_o^0$ is obtained by minimizing (35) and $\bar{\chi}_b^1 = \bar{\chi}_o^0$.

Step 2: $n = n + 1$.

Update the secondary incident field in the general background

$$\bar{E}_b^{p,n} = (\bar{I} - \bar{\bar{G}}_D \cdot \bar{\chi}_b^n)^{-1} \cdot \bar{E}_{\text{inc}}^p \quad (41)$$

$$\bar{E}_{b,\text{TID}}^{p,n} = (\bar{I} - \bar{\bar{G}}_{D,\text{TID}} \cdot \bar{\chi}_{b,\text{TID}}^n)^{-1} \cdot \bar{E}_{\text{inc},\text{TID}}^p \quad (42)$$

$$\bar{E}_{b,R}^{p,n} = \bar{E}_{\text{inc},R}^p + \bar{\bar{G}}_s \cdot \bar{\chi}_b^n \cdot \bar{E}_b^{p,n}. \quad (43)$$

Update $\bar{\psi}_R^{p,n}$

$$\bar{\psi}_R^{p,n}(m) = \ln \left(\bar{E}_{t,R}^p(m) / \bar{E}_{b,R}^{p,n}(m) \right). \quad (44)$$

Update background Green's function $\bar{\bar{G}}_{\text{bs}}^n$, $\bar{\bar{G}}_{\text{bs},\text{TID}}^n$, and $\bar{\bar{G}}_{b,D,\text{TID}}^n$

$$\bar{\bar{G}}_{\text{bs}}^n = \bar{\bar{G}}_s \cdot (\bar{I} - \bar{\chi}_b^n \cdot \bar{\bar{G}}_D)^{-1} \quad (45)$$

$$\bar{\bar{G}}_{\text{bs},\text{TID}}^n = \bar{\bar{G}}_{\text{s,TID}}^0 \cdot (\bar{I} - \bar{\chi}_{b,\text{TID}}^n \cdot \bar{\bar{G}}_{D,\text{TID}}^0)^{-1} \quad (46)$$

$$\bar{\bar{G}}_{b,D,\text{TID}}^n = \bar{\bar{G}}_{D,\text{TID}}^0 \cdot (\bar{I} - \bar{\chi}_{b,\text{TID}}^n \cdot \bar{\bar{G}}_{D,\text{TID}}^0)^{-1}. \quad (47)$$

Calculate the thin SVD of \bar{G}_{bs}^n in (45)

$$\bar{G}_{\text{bs}}^n = \sum_{i=1}^{N_s} \sigma_{i,n} \cdot \bar{u}_{i,n} \cdot \bar{v}_{i,n}^H. \quad (48)$$

Calculate the major part of the induced current

$$\bar{J}_+^{p,n} = \sum_{i=1}^L \frac{\bar{u}_{i,n}^H \cdot (\bar{E}_{t,R}^p - \bar{E}_{\text{inc},R}^p - \bar{G}_s \cdot \bar{\chi}_b^n \cdot \bar{E}_b^{p,n})}{\sigma_{i,n}} \bar{v}_{i,n} \quad (49)$$

next, $\bar{J}_{+, \text{TID}}^{p,n}$ is obtained by padding zeros to $\bar{J}_+^{p,n}$.

Update $\bar{E}_{\text{sa,TID}}^{p,n}$, $\bar{E}_{\text{ta,TID}}^{p,n}$

$$\bar{E}_{\text{sa,TID}}^{p,n} = \bar{G}_{b,\text{TID}}^n \cdot \bar{J}_{+, \text{TID}}^{p,n} \quad (50)$$

$$\bar{E}_{\text{ta,TID}}^{p,n} = \bar{E}_{b,\text{TID}}^{p,n} + \bar{E}_{\text{sa,TID}}^{p,n}. \quad (51)$$

Update $\bar{P}_{2,\text{TID}}^{p,n}$

$\bar{P}_{2,\text{TID}}^{p,n}(m, m)$

$$= \left[\begin{array}{l} \bar{G}_{x,\text{TID}}^m \cdot (\bar{I} - \bar{\chi}_{b,\text{TID}}^n \cdot \bar{G}_{D,\text{TID}}) \cdot \bar{J}_{+, \text{TID}}^{p,n} \cdot \bar{E}_{b,\text{TID}}^{p,n}(m) \\ -ik \cos(\theta_{\text{inc}}) \bar{E}_{\text{inc},\text{TID}}^p(m) \bar{E}_{\text{sa,TID}}^{p,n}(m) \\ -\bar{G}_{x,\text{TID}}^m \cdot \bar{\chi}_{b,\text{TID}}^n \cdot \bar{E}_{b,\text{TID}}^{p,n} \bar{E}_{\text{sa,TID}}^{p,n}(m) \\ + \bar{G}_{y,\text{TID}}^m \cdot (\bar{I} - \bar{\chi}_{b,\text{TID}}^n \cdot \bar{G}_{D,\text{TID}}) \cdot \bar{J}_{+, \text{TID}}^{p,n} \cdot \bar{E}_{b,\text{TID}}^{p,n}(m) \\ -ik \sin(\theta_{\text{inc}}) \bar{E}_{\text{inc},\text{TID}}^p(m) \bar{E}_{\text{sa,TID}}^{p,n}(m) \\ -\bar{G}_{y,\text{TID}}^m \cdot \bar{\chi}_{b,\text{TID}}^n \cdot \bar{E}_{b,\text{TID}}^{p,n} \bar{E}_{\text{sa,TID}}^{p,n}(m) \end{array} \right]^2 / (\bar{E}_{\text{ta,TID}}^{p,n}(m) \cdot \bar{E}_{b,\text{TID}}^{p,n}(m))^2. \quad (52)$$

Step 3: Update $\bar{\chi}_o^n$ by minimizing (35) and update the normalized contrast by

$$\bar{\chi}_b^{n+1} = \bar{\chi}_b^n + \bar{\chi}_o^n. \quad (53)$$

Step 4: If the termination condition is satisfied, end the loop. Otherwise, go to Step 2.

III. COMPUTATIONAL COMPLEXITY

In this proposed S-DRIM, the additional cost compared with the DRIM is associated with the retained term, i.e., $(1/i\omega\mu_0)\bar{G}_{\text{bs},\text{TID}}^n \cdot \bar{P}_{2,\text{TID}}^{p,n} \cdot \bar{E}_{b,\text{TID}}^{p,n}$. In the retained term, the following computations are involved.

- 1) We do not have to calculate $\bar{G}_{\text{bs},\text{TID}}^n$ explicitly because it always appears in a matrix-vector product, which can be accelerated by the FFT algorithm at a very low computational cost of $O(M_{\text{TID}} \log M_{\text{TID}} + M_{\text{TID}} N_s)$.
- 2) $\bar{E}_{b,\text{TID}}^{p,n}$ is also computed using the FFT algorithm and the computational cost is $O(M_{\text{TID}} \log M_{\text{TID}})$.
- 3) The computation cost associated with $\bar{P}_{2,\text{TID}}^{p,n}$ is dominated by the computation of \bar{G}_{bs}^n , the thin SVD of \bar{G}_{bs}^n and the computation of $(\bar{I} - \bar{\chi}_{b,\text{TID}}^n \cdot \bar{G}_{D,\text{TID}})^{-1} \cdot \bar{J}_{+, \text{TID}}^{p,n}$.
 - a) \bar{G}_{bs}^n is computed using the reciprocity theorem and the computational cost is $O(N_s M_{\text{DOI}} \log M_{\text{DOI}})$.

- b) The computational cost of the thin SVD of \bar{G}_{bs}^n is $O(N_s^2 M_{\text{DOI}})$.
- c) The computational cost of $(\bar{I} - \bar{\chi}_{b,\text{TID}}^n \cdot \bar{G}_{D,\text{TID}})^{-1} \cdot \bar{J}_{+, \text{TID}}^{p,n}$ is $O(M_{\text{TID}} \log M_{\text{TID}})$ by using the FFT algorithm to replace the matrix inversion.

Therefore, the computational cost of $\bar{P}_{2,\text{TID}}^{p,n}$ is $O(N_s M_{\text{DOI}} \log M_{\text{DOI}} + N_s^2 M_{\text{DOI}} + M_{\text{TID}} \log M_{\text{TID}})$.

To summarize, the additional computational cost of S-DRIM is $O(N_s M_{\text{DOI}} \log M_{\text{DOI}} + N_s^2 M_{\text{DOI}} + M_{\text{TID}} \log M_{\text{TID}} + M_{\text{TID}} N_s)$.

IV. NUMERICAL RESULTS

A. Errors of RA in a General Background

It is well known that the RA is not applicable for strong scatterers in the free space background, for which the condition of $(\nabla' \psi)^2 \ll i\omega\mu_0\chi_o$ is not satisfied. However, the DRIM has been widely used for inversions of strong scatterers in the free space. In each iteration of the DRIM, the background is updated. The DRIM is supposed to converge to a point, where the value of the cost function is small and the background is close to the ground truth. In other words, when the permittivity distribution of the background medium is close to that of the scatterer, a small error should be caused by the RA. Therefore, in this section, for verification, the error caused by the RA, which is defined in (16), is calculated for different scatterers in different background mediums with only small permittivity deviation within the regions of the scatterers.

In Sections IV-A–IV-C, the scatterers are illuminated by 16 incidences of frequency 400 MHz. About 32 observation points are uniformly located on a scatterer-centered circle of radius 3 m. The size of the DOI is 2 × 2 m. In this section, the Austria ring scatterers with different values of permittivity are used. Assume that the relative permittivity of the scatterer is $\epsilon_{\text{or}}(\mathbf{r}')$, the relative permittivity of the background medium is $\epsilon_{\text{br}}(\mathbf{r}') = \epsilon_{\text{or}}(\mathbf{r}') - 0.1$ for \mathbf{r}' inside the scatterer and $\epsilon_{\text{br}}(\mathbf{r}') = 1$ for \mathbf{r}' outside of the scatterer. The error caused by the RA in the background, which is defined in (16), is plotted in Fig. 2. In Fig. 2, the normalized contrast of the scatterer, which is defined as $\chi_o(\mathbf{r}') = -i\omega\epsilon_0[\epsilon_{\text{or}}(\mathbf{r}') - \epsilon_{\text{br}}(\mathbf{r}')]$, is kept as a constant for \mathbf{r}' inside the scatterer. The normalized contrast of the background, which is defined as $\chi_b(\mathbf{r}) = -i\omega\epsilon_0[\epsilon_{\text{br}}(\mathbf{r}) - 1]$, is increased for \mathbf{r}' inside the scatterer. It can be seen that when the relative permittivity difference between the background and the scatterer is small, the RA is accurate even for a scatterer with high permittivity.

B. Errors of SRA in a General Background Using Different Sizes of TID

In this section, to see how the accuracy of the SRA in a general background will vary with increasing area of the TID, err_1 and err_2 , which are defined in (23) and (27), respectively, are calculated for different sizes of TID.

We consider an Austria ring with relative permittivity of 1.4 placed in the free space. The relative permittivity of background medium is 1.3 within the Austria ring and it is 1 outside the Austria ring. The major induced current in

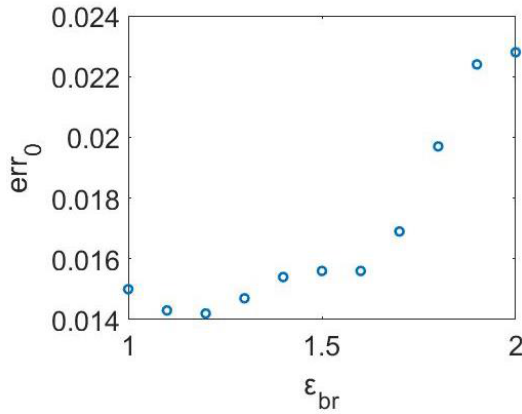


Fig. 2. Approximation errors defined in (16) for Austria ring scatterers with different relative permittivity in different background mediums. $\varepsilon_{br}(r') = \varepsilon_{sr}(r') - 0.1$ for r' inside the scatterer.

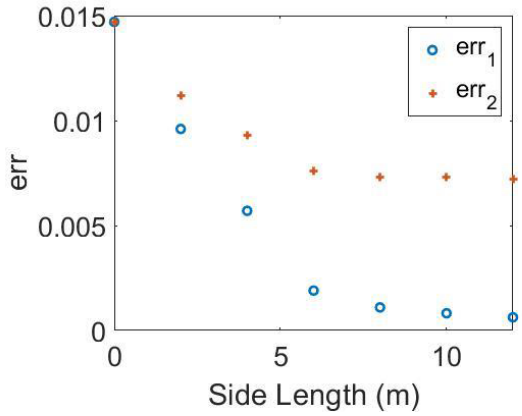


Fig. 3. Approximation errors defined in (23) and (27) using different sizes of TID.

err_2 is calculated using $L=15$. err_1 and err_2 are plotted in Fig. 3 with increasing TID side length from 0 to 12 m. When the side length of the TID is 0, it means that the RA is used. First, it can be seen from Fig. 3 that the SRA is applicable in the inhomogeneous background and it is more accurate than the RA by retaining the neglected term. Second, both err_1 and err_2 are diminishing with increasing TID side length. By retaining and approximating the neglected term in RA using the complete induced current, err_1 is approaching zero with increasing the side length of the TID. err_2 , which retains and approximates the neglected term using the major induced current is approaching a small value of approximation error. The decreasing trends of the approximation errors are negligible when the side length of the TID is several times larger than the side length of the DOI. Third, we find in a lot of simulations that, analogous to the example, mild scatterers usually require a relatively small scatterer-centered TID to achieve a good approximation of the retained integral term. In comparison, for strong scatterers, a large TID is demanded to obtain a reasonable approximation of the retained term.

C. Comparison of Errors Using RA and SRA

In the DRIM, the RA is used in each iteration with updated background. With an increasing number of iterations, the

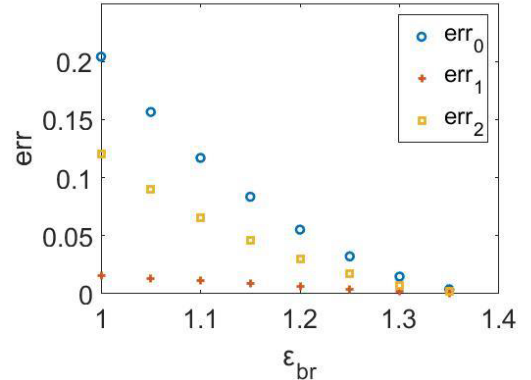


Fig. 4. Approximation errors defined in (16), (23), and (27) for an Austria ring scatterer with relative permittivity of 1.4 for various background mediums that we choose.

background medium is getting closer to the ground truth. It is of our interest to see the variation trend of the approximation error of the RA, which is defined in (16), with the decreasing difference between the background medium and the ground truth. To apply the SRA in the iterative inversion method, it is also worthwhile to see the variation of the approximation error of the SRA, which is defined in (27), with decreasing difference between the background medium and the ground truth. In this section, the approximation errors of both the RA and the SRA, which are defined in (16) and (27), respectively, are calculated for a fixed scatterer with varying differences between the permittivity distribution of the background medium and the scatterer.

In this section, an Austria ring scatterer [37] with relative permittivity $\varepsilon_{sr}=1.4$ is used. The relative permittivity of the background medium is ε_{br} within the scatterer and it is 1 outside the scatterer. When ε_{br} is increased from 1 to 1.35, the corresponding approximation errors, which are defined in (16), (23) and (27), are plotted in Fig. 4. For err_2 of the SRA in (27), $L=15$ is used for the major induced current and the side length of the TID is 6 m. We mainly have two observations. First, it can be seen that when ε_{br} is getting close to ε_{sr} , the approximation errors of the RA and the SRA are decreasing. Second, the SRA has a higher accuracy than the RA, however, the advantage of the SRA is weakened when ε_{br} is getting close to ε_{sr} . Both the RA and SRA are quite accurate when $\varepsilon_{br}-\varepsilon_{sr}$ is small.

D. Tests With Austria Ring Profile

In Sections IV-D and IV-E, the same measurement setup is used. About 16 incident plane waves at the frequency of 400 MHz are used and 32 receivers are located on a circle of radius 3 m with equal angular separations. The DOI, of which the side length is 2m, is discretized into 64×64 pixels. The TID, of which the side length is 6 m, is discretized into 192×192 pixels. The scattered field is contaminated by the additive white Gaussian noise (AWGN) and the noise level is defined as $\|\bar{n}\|_F/\|\bar{E}_s\|_F$, where \bar{E}_s and \bar{n} are of size $N_s \times N_t$. In the convergence curves, $\log_{10}(g)$ is plotted, where $g = \|\bar{\epsilon}_{r,gt} - \bar{\epsilon}_{r,rec}\|_F/\|\bar{\epsilon}_{r,gt}\|_F$, where $\bar{\epsilon}_{r,gt}$ is the relative permittivity of the ground truth and $\bar{\epsilon}_{r,rec}$ is the relative

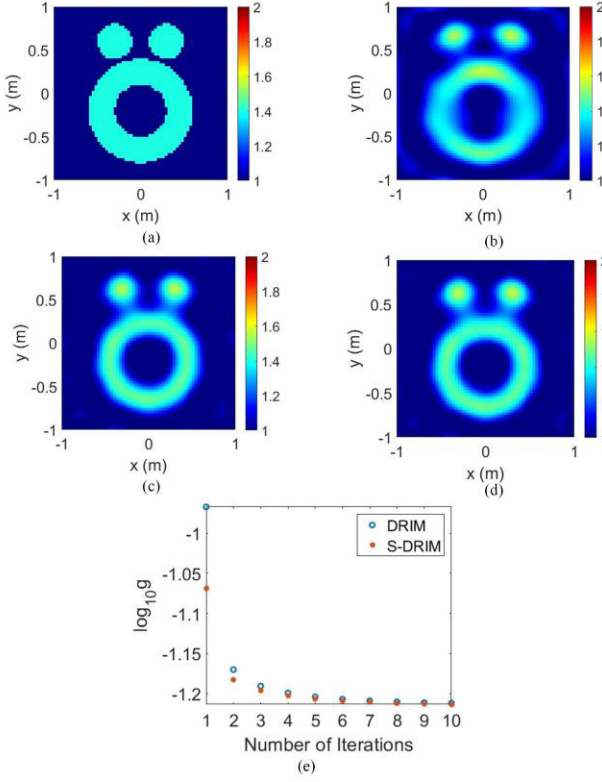


Fig. 5. (a) Austria ring profile with relative permittivity of 1.4, reconstructed profile using (b) non-iterative SRA inversion method, (c) DRIM, (d) S-DRIM, and (e) convergence curves using DRIM and S-DRIM.

permittivity of the reconstruction. Both $\bar{\varepsilon}_{r,gt}$ and $\bar{\varepsilon}_{r,rec}$ are of length M_{DOI} .

In this section, an Austria ring with relative permittivity of 1.4, which is plotted in Fig. 5(a), is used. The scattered field is contaminated by 5% AWGN. The reconstruction results using the non-iterative SRA inversion method, DRIM, and S-DRIM are plotted in Fig. 5(b)–(d), respectively. The reconstructed profile of the non-iterative SRA inversion method is the reconstruction result after the first iteration using S-DRIM. It can be seen from the convergence curves in Fig. 5(e) that both the S-DRIM and DRIM have a better performance than the non-iterative SRA inversion method. At the initial stage of the inversion, the S-DRIM has a better performance than the DRIM. The advantage of the S-DRIM vanishes gradually as the permittivity distribution of the background medium gets closer to that of the scatterer. It is consistent with the simulation results in Section III-B. In the first few iterations, the big difference between the permittivity distributions of the scatterer and the background medium leads to advantage of the SRA over the RA in accuracy. Hence, the S-DRIM has a lower value of reconstruction error than the DRIM at the initial stage. When the difference between the permittivity distributions of the scatterer and the background medium is small, the RA is almost as accurate as the SRA and the convergence rates of the DRIM and the S-DRIM are similar. The relative errors of the reconstructions using different methods are given in the second column of Table II.

TABLE II
RELATIVE ERRORS USING DIFFERENT METHODS

	Austria Ring	Alphabetic	Square	Experiment
SRA	8.54%	8.11%	7.68%	30.99%
DRIM	6.14%	6.48%	5.99%	21.31%
S-DRIM	6.12%	6.44%	6.00%	21.25%

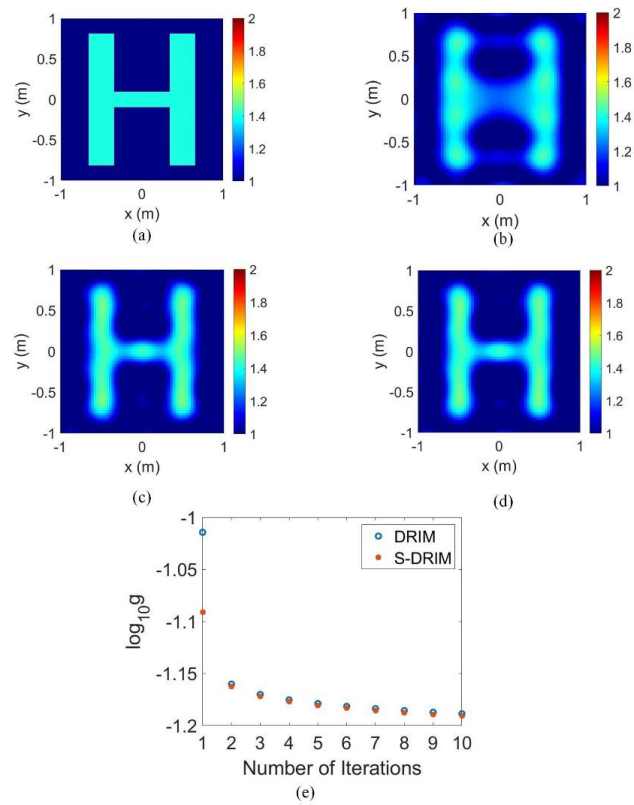


Fig. 6. (a) Alphabetic profile with relative permittivity of 1.4, reconstructed profile using (b) non-iterative SRA inversion method, (c) DRIM, (d) S-DRIM, and (e) convergence curves using DRIM and S-DRIM.

E. Test With Alphabetic Profile

In this section, an alphabetic profile with relative permittivity of 1.4 is used. The scattered field is contaminated by 5% AWGN. The ground truth of the scatterer is shown in Fig. 6(a). The inversion results using the non-iterative SRA inversion method, DRIM, and S-DRIM are shown in Fig. 6(b)–(d), respectively. The convergences curves of different iterative methods are shown in Fig. 6(e). Both the DRIM and S-DRIM outperform the non-iterative SRA inversion method. At the beginning of the inversion process, the S-DRIM has a lower reconstruction error than the DRIM. The relative errors of the reconstructions using different methods are given in the third column of Table II.

F. Tests With Square Profile

In this section, a square profile with relative permittivity of 1.4 is used. The scattered field is contaminated by 30% AWGN. The ground truth profile is plotted in Fig. 7(a). The reconstructions using the non-iterative SRA inversion method, the DRIM, and the S-DRIM are plotted in

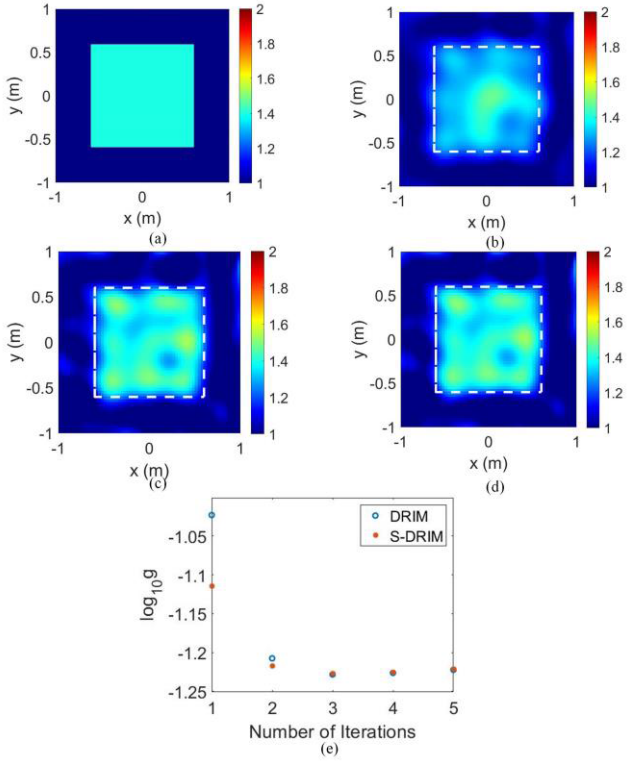


Fig. 7. (a) Square profile with relative permittivity of 1.4, reconstructed profile using (b) non-iterative SRA inversion method, (c) DRIM, (d) S-DRIM, and (e) convergence curves using DRIM and S-DRIM.

Fig. 7(b)–(d), respectively. The convergence curves of the DRIM and the S-DRIM are plotted in Fig. 7(e). It can be seen from the simulation results that the proposed S-DRIM is robust against high noise level. Both the DRIM and the S-DRIM outperform the non-iterative SRA inversion method. During the early stage of the inversion process, the S-DRIM has a lower reconstruction error than the DRIM. And the final reconstruction results of both iterative methods are similar to each other. The relative errors of the reconstructions using different methods are given in the fourth column of Table II.

G. Tests With Experiment Data

In this section, experiment data [38] are used to test the performance of the proposed method.

In the experiment, the scatterer is a cylinder with relative permittivity of 3 ± 0.3 and a radius of 0.015 m as shown in Fig. 8(a). The operating frequency is 3 GHz. The DOI, of which the side length is 0.1 m, is discretized into 64×64 pixels. The TID, of which the side length is 0.3 m, is discretized into 192×192 pixels. The transmitter is rotated around the scatterer with a radius of 0.72 ± 0.003 m and the receiver is rotated around the scatterer with a radius of 0.76 ± 0.003 m. 36 incidences are used in total. For each incidence, the scattered field is measured at 49 different locations and the minimum angle between the directions from the origin to the transmitting and the receiving antennas is 60° . The reconstructions of the non-iterative SRA inversion method, DRIM, and S-DRIM are plotted in Fig. 8(b)–(d),

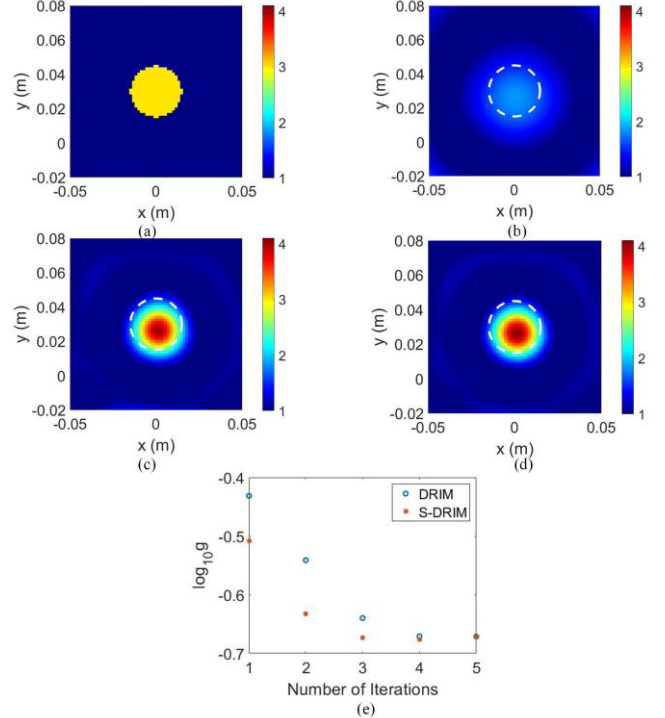


Fig. 8. (a) Experiment profile with relative permittivity of 3.0, reconstructed profile using (b) non-iterative SRA inversion method, (c) DRIM, (d) S-DRIM, and (e) convergence curves using DRIM and S-DRIM.

respectively. The convergence curves of the DRIM and S-DRIM are plotted in Fig. 8(e). It can be seen that both DRIM and S-DRIM outperform the non-iterative SRA inversion method. The S-DRIM has a lower reconstruction error than the DRIM at the beginning of the inversion process. The reconstructions of the DRIM and the S-DRIM are similar to each other. The relative errors of the reconstructions using different methods are given in the fifth column of Table II.

V. CONCLUSION AND DISCUSSION

In this article, we have proposed a new iterative method, called the S-DRIM, to solve inverse scattering problems. In each iteration of the S-DRIM, the SRA is used to do the inversion in an iteratively updated background.

The contributions of this article are as follows. First, the performance of the RA and the SRA is compared in the background. It is observed that the RA and the SRA are both accurate when the permittivity distribution of the background is close to that of the scatterer. The SRA outperforms the RA when the difference between the permittivity distributions of the scatterer and the background medium is large. Second, the S-DRIM outperforms the non-iterative SRA inversion method for mild scatterers, since the non-iterative SRA inversion method is the first iteration of the S-DRIM. Third, in the inversion process, the S-DRIM has a lower reconstruction error than the DRIM. This is consistent with the observation that the SRA is more accurate than the RA when there is a significant difference between the permittivity distribution of the scatterer and the background medium and the advantage

gradually decreases as the difference is getting smaller. Fourth, the approximation errors of the RA and the SRA are defined in a new way to avoid the phase wrapping problems that might be encountered for strong scatterers.

Due to the huge TID requirement for high-contrast scatterers, the S-DRIM incurs both high computational costs and extensive memory usage to solve inverse scattering problems. As a result, the inversion results for high-contrast scatterers are not provided in this article, given the limitations of our computational platform. Our future work aims at integrating the insights on wave physics discussed in this article with machine learning techniques to address both the electromagnetic scattering forward problem and the inverse problem [39].

REFERENCES

- [1] M. Slaney, A. C. Kak, and L. E. Larsen, "Limitations of imaging with first-order diffraction tomography," *IEEE Trans. Microw. Theory Techn.*, vol. MTT-32, no. 8, pp. 860–874, Aug. 1984.
- [2] B. Chen and J. J. Stammes, "Validity of diffraction tomography based on the first Born and the first Rytov approximations," *Appl. Opt.*, vol. 37, no. 14, pp. 2996–3006, May 1998.
- [3] A. J. Devaney, "Inverse-scattering theory within the Rytov approximation," *Opt. Lett.*, vol. 6, no. 8, pp. 374–376, Aug. 1981.
- [4] K. Belkebir, P. C. Chaumet, and A. Sentenac, "Superresolution in total internal reflection tomography," *J. Opt. Soc. Amer. A, Opt. Image Sci.*, vol. 22, no. 9, pp. 1889–1897, 2005.
- [5] S. Depatla, L. Buckland, and Y. Mostofi, "X-ray vision with only WiFi power measurements using Rytov wave models," *IEEE Trans. Veh. Technol.*, vol. 64, no. 4, pp. 1376–1387, Apr. 2015.
- [6] Y. Sung and G. Barbastathis, "Rytov approximation for X-ray phase imaging," *Opt. Exp.*, vol. 21, no. 3, pp. 2674–2682, Feb. 2013.
- [7] O. Sasaki and T. Kobayashi, "Beam-deflection optical tomography of the refractive-index distribution based on the Rytov approximation," *Appl. Opt.*, vol. 32, no. 5, pp. 746–751, Feb. 1993.
- [8] T. E. Gureyev, T. J. Davis, A. Pogany, S. C. Mayo, and S. W. Wilkins, "Optical phase retrieval by use of first Born- and Rytov-type approximations," *Appl. Opt.*, vol. 43, no. 12, pp. 2418–2430, Apr. 2004.
- [9] K. Zhang, Z. Yin, Z.-C. Li, and Y.-R. Chen, "Wave equation tomographic velocity inversion method based on the Born/Rytov approximation," *Appl. Geophys.*, vol. 10, no. 3, pp. 314–322, Sep. 2013.
- [10] W. Wang, L. Jing, Z. Li, and R. D. Murch, "Utilizing the Born and Rytov inverse scattering approximations for detecting soft faults in lossless transmission lines," *IEEE Trans. Antennas Propag.*, vol. 65, no. 12, pp. 7233–7243, Dec. 2017.
- [11] T. M. Habashy, R. W. Groom, and B. R. Spies, "Beyond the Born and Rytov approximations: A nonlinear approach to electromagnetic scattering," *J. Geophys. Res., Solid Earth*, vol. 98, no. 2, pp. 1759–1775, Feb. 1993.
- [12] T. Yin, Z. Wei, and X. Chen, "Non-iterative methods based on singular value decomposition for inverse scattering problems," *IEEE Trans. Antennas Propag.*, vol. 68, no. 6, pp. 4764–4773, Jun. 2020.
- [13] D. L. Marks, "A family of approximations spanning the Born and Rytov scattering series," *Opt. Exp.*, vol. 14, no. 19, pp. 8837–8848, Sep. 2006.
- [14] A. Dubey, S. Deshmukh, L. Pan, X. Chen, and R. Murch, "A phaseless extended Rytov approximation for strongly scattering low-loss media and its application to indoor imaging," *IEEE Trans. Geosci. Remote Sens.*, vol. 60, 2022, Art. no. 2005017.
- [15] T. Yin, L. Pan, and X. Chen, "Subspace-Rytov approximation inversion method for inverse scattering problems," *IEEE Trans. Antennas Propag.*, vol. 70, no. 11, pp. 10925–10935, Nov. 2022.
- [16] P. M. V. D. Berg, A. L. V. Broekhoven, and A. Abubakar, "Extended contrast source inversion," *Inverse Problems*, vol. 15, no. 5, pp. 1325–1344, Oct. 1999.
- [17] X. Chen, "Subspace-based optimization method for solving inverse-scattering problems," *IEEE Trans. Geosci. Remote Sens.*, vol. 48, no. 1, pp. 42–49, Jan. 2010.
- [18] T. Yin, Z. Wei, and X. Chen, "Wavelet transform subspace-based optimization method for inverse scattering," *IEEE J. Multiscale Multiphys. Comput. Techn.*, vol. 3, pp. 176–184, 2018.
- [19] T. Isernia, L. Crocco, and M. D'Urso, "New tools and series for forward and inverse scattering problems in lossy media," *IEEE Geosci. Remote Sens. Lett.*, vol. 1, no. 4, pp. 327–331, Oct. 2004.
- [20] W. C. Chew and Y. M. Wang, "Reconstruction of two-dimensional permittivity distribution using the distorted Born iterative method," *IEEE Trans. Med. Imag.*, vol. 9, no. 2, pp. 218–225, Jun. 1990.
- [21] S. Y. Semenov et al., "Microwave tomography: Theoretical and experimental investigation of the iteration reconstruction algorithm," *IEEE Trans. Microw. Theory Techn.*, vol. 46, no. 2, pp. 133–141, Feb. 1998.
- [22] W. Zhang and A. Hoofar, "Reconstruction of two-dimensional permittivity distribution with distorted Rytov iterative method," *IEEE Antennas Wireless Propag. Lett.*, vol. 10, pp. 1072–1075, 2011.
- [23] W. Zhang, L. Li, and F. Li, "Multifrequency imaging from intensity-only data using the phaseless data distorted Rytov iterative method," *IEEE Trans. Antennas Propag.*, vol. 57, no. 1, pp. 290–295, Jan. 2009.
- [24] L. Li, W. Zhang, and F. Li, "Tomographic reconstruction using the distorted Rytov iterative method with phaseless data," *IEEE Geosci. Remote Sens. Lett.*, vol. 5, no. 3, pp. 479–483, Jul. 2008.
- [25] C. N. Kechribaris, K. S. Nikita, and N. K. Uzunoglu, "Reconstruction of two-dimensional permittivity distribution using an improved Rytov approximation and nonlinear optimization," *J. Electromagn. Waves Appl.*, vol. 17, no. 2, pp. 183–207, Jan. 2003.
- [26] A. Dubey and R. Murch, "Distorted wave extended phaseless Rytov iterative method for inverse scattering problems," 2022, *arXiv:2205.12578*.
- [27] G. Oliveri, Y. Zhong, X. Chen, and A. Massa, "Multiresolution subspace-based optimization method for inverse scattering problems," *J. Opt. Soc. Amer. A, Opt. Image Sci.*, vol. 28, no. 10, pp. 2057–2069, Oct. 2011.
- [28] X. Ye et al., "Multi-resolution subspace-based optimization method for solving three-dimensional inverse scattering problems," *J. Opt. Soc. Amer. A, Opt. Image Sci.*, vol. 32, no. 11, pp. 2218–2226, Nov. 2015.
- [29] Y. Zhong, M. Salucci, K. Xu, A. Polo, and A. Massa, "A multiresolution contraction integral equation method for solving highly nonlinear inverse scattering problems," *IEEE Trans. Microw. Theory Techn.*, vol. 68, no. 4, pp. 1234–1247, Apr. 2020.
- [30] Y. Zhong, M. Lambert, D. Lesselier, and X. Chen, "A new integral equation method to solve highly nonlinear inverse scattering problems," *IEEE Trans. Antennas Propag.*, vol. 64, no. 5, pp. 1788–1799, May 2016.
- [31] L. Manica, P. Rocca, M. Salucci, M. Carlin, and A. Massa, "Scattering data inversion through interval analysis under Rytov approximation," in *Proc. 7th Eur. Conf. Antennas Propag. (EuCAP)*, Apr. 2013, pp. 82–85.
- [32] S. Caorsi, A. Massa, and M. Pastorino, "Rytov approximation: Application to scattering by two-dimensional weakly nonlinear dielectrics," *J. Opt. Soc. Amer. A, Opt. Image Sci.*, vol. 13, no. 3, pp. 509–516, Mar. 1996.
- [33] G. A. Tsirhrintzis and A. J. Devaney, "Higher order (nonlinear) diffraction tomography: Inversion of the Rytov series," *IEEE Trans. Inf. Theory*, vol. 46, no. 5, pp. 1748–1761, Aug. 2000.
- [34] G. Oliveri, L. Poli, P. Rocca, and A. Massa, "Bayesian compressive optical imaging within the Rytov approximation," *Opt. Lett.*, vol. 37, no. 10, pp. 1760–1762, May 2012.
- [35] G. Beylkin and M. L. Oristaglio, "Distorted-wave Born and distorted-wave Rytov approximations," *Opt. Commun.*, vol. 53, no. 4, pp. 213–216, Mar. 1985.
- [36] X. Ye and X. Chen, "Subspace-based distorted-Born iterative method for solving inverse scattering problems," *IEEE Trans. Antennas Propag.*, vol. 65, no. 12, pp. 7224–7232, Dec. 2017.
- [37] X. Chen, *Computational Methods for Electromagnetic Inverse Scattering*. Singapore: Wiley, 2018.
- [38] K. Belkebir and M. Saillard, "Testing inversion algorithms against experimental data," *Inverse Problems*, vol. 17, no. 6, pp. 1565–1571, Nov. 2001.
- [39] T. Yin, C.-F. Wang, K. Xu, Y. Zhou, Y. Zhong, and X. Chen, "Electric flux density learning method for solving 3-D electromagnetic scattering problems," *IEEE Trans. Antennas Propag.*, vol. 70, no. 7, pp. 5144–5155, Jul. 2022.



Tiantian Yin received the B.E. degree (Hons.) in electrical and electronic engineering from Nanyang Technological University, Singapore, in 2016, and the Ph.D. degree in electrical and computer engineering from the National University of Singapore, Singapore, in 2021.

She is currently a Research Fellow with the National University of Singapore. Her research interests include electromagnetic inverse scattering problems.

Dr. Yin was a recipient of the 2020 Best Student Paper Competition Award from the IEEE Singapore Microwave Theory and Techniques/Antennas and Propagation (MTT/AP) Chapter.



Li Pan (Member, IEEE) received the B.Sc. degree in electrical and computer engineering (ECE) from Zhejiang University, Hangzhou, China, in 2003, the M.Sc. degree in ECE from the Chalmers University of Technology, Gothenburg, Sweden, in 2006, and the Ph.D. degree in ECE from the National University of Singapore, Singapore, in 2011.

He worked with the Department of Sensor Physics, Halliburton, Singapore, from 2012 to 2022, where he developed various electromagnetic (EM) forward modeling and inversion algorithms for the novel EM based downhole formation evaluation services for oil and gas reservoir detection. He joined Huawei, Singapore, in 2022, as an Expert in EM sensing, and his work involves the research and development in the area of integrated sensing and communication (ISAC) for 6G. His research interests include numerical methods for EM modeling and inverse problems.



Xudong Chen (Fellow, IEEE) received the B.S. and M.S. degrees from Zhejiang University, Hangzhou, China, in 1999 and 2001, respectively, and the Ph.D. degree from the Massachusetts Institute of Technology, Cambridge, MA, USA, in 2005.

Since 2005, he has been with the National University of Singapore, Singapore, where he is currently a Professor. He has published 170 journal articles on inverse scattering problems, material parameter retrieval, microscopy, optical encryption, and physics-assisted machine learning. He has authored the book *Computational Methods for Electromagnetic Inverse Scattering* (Wiley-IEEE, 2018). His research interests include mainly electromagnetic wave theories and applications, with a focus on inverse problems and computational imaging.

Dr. Chen is a Fellow of the Electromagnetics Academy. He was a recipient of the Young Scientist Award by the Union Radio Scientifique Internationale in 2010 and the Ulrich L. Rohde Innovative Conference Paper Award at International Conference on Computational Electromagnetics (ICCEM) 2019 Conference. He has been member of organizing committees of more than ten conferences, serving as a General Chair, a Technical Program Committee (TPC) Chair, and the Award Committee Chair. He was the Chair of IEEE Singapore Microwave Theory and Techniques (MTT)/Antennas and Propagation (AP) Joint Chapter in 2018. He was an Associate Editor of IEEE TRANSACTIONS ON MICROWAVE THEORY AND TECHNIQUES and IEEE TRANSACTIONS ON GEOSCIENCE AND REMOTE SENSING (TGRS). He is currently a Deputy Editor-in-Chief (D-EiC) of IEEE TGRS and an Associate Editor (AE) of IEEE JOURNAL OF ELECTROMAGNETICS, RF, AND MICROWAVES IN MEDICINE AND BIOLOGY.